Natural Hazards
and Earth System
Sciences

Open Access

Supplement of

Projected intensification of sub-daily and daily rainfall extremes in convection-permitting climate model simulations over North America: implications for future intensity–duration–frequency curves

Alex J. Cannon and Silvia Innocenti

Correspondence to: Alex J. Cannon (alex.cannon@canada.ca)
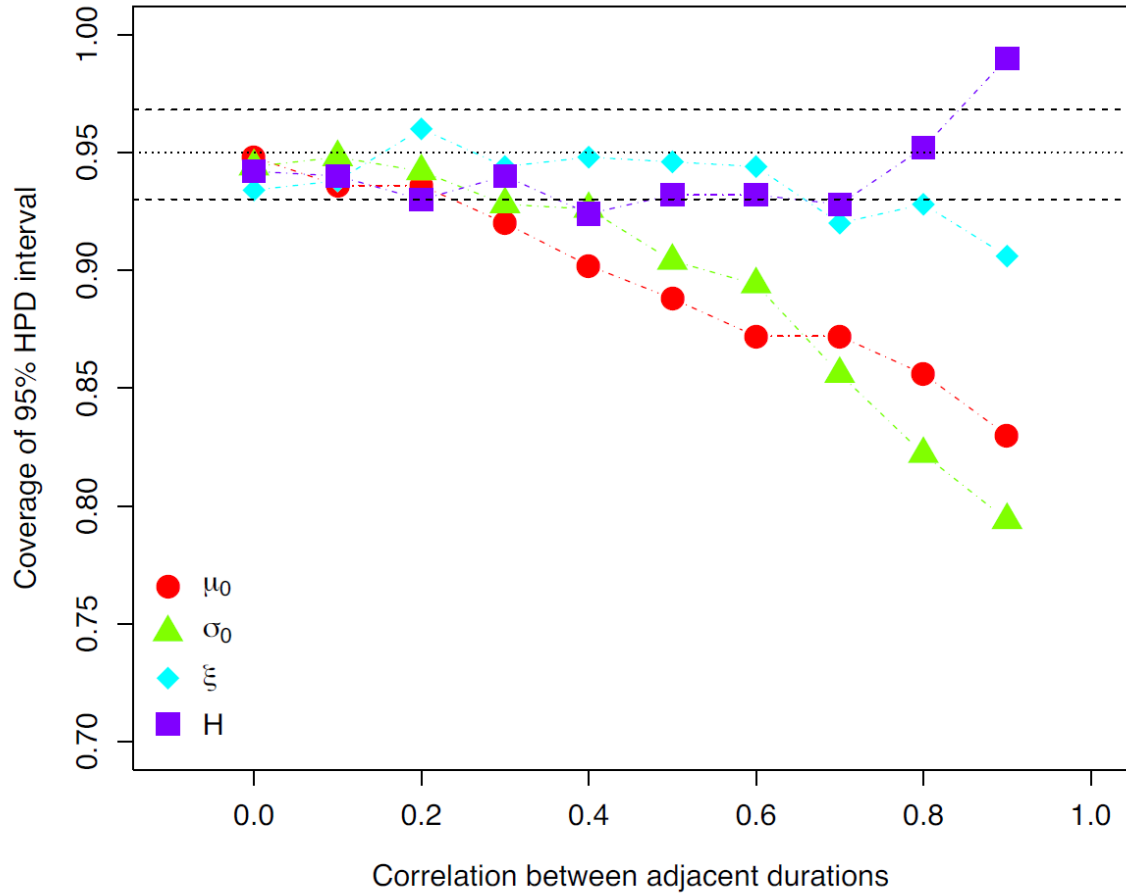
Figure S1: Coverage of 95% Highest Posterior Density (HPD) credible intervals for fitted GEVSS location μ_0, scale σ_0, shape ξ, and scaling exponent H parameters based on 501 Monte Carlo simulations from the same specified GEVSS distribution – with parameters drawn from the prior distributions in Section 4 – but with different levels of correlation between adjacent simulated accumulation durations (i.e., lack of independence). The sample size is set to 13-yr to match the length of the WRF simulations. The nominal coverage level is shown by the dotted horizontal line, with dashed lines showing the 95% acceptance region based on 501 Monte Carlo simulations.
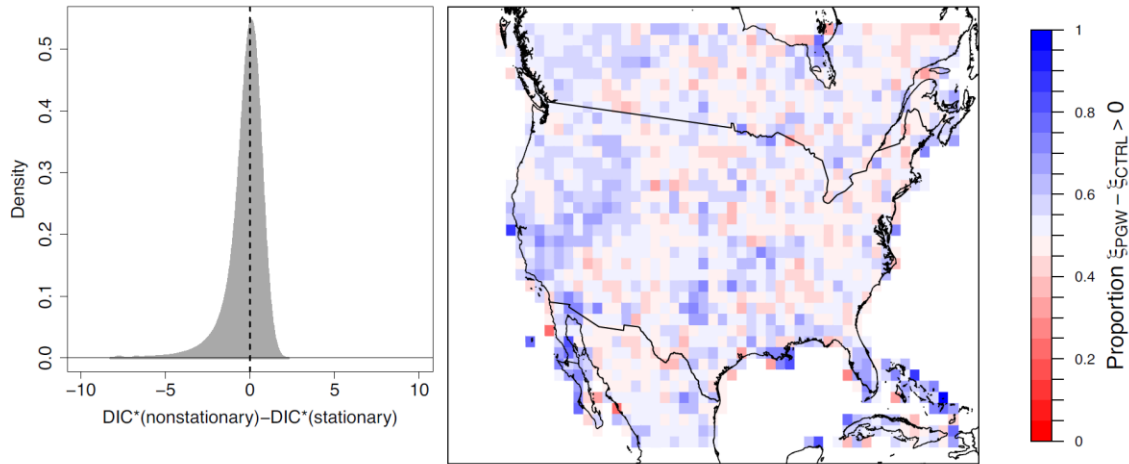
Figure S2: Lesaffre and Lawson (2012) state that "The rule of thumb for using DIC in model selection is roughly the same as for AIC and BIC, namely, a difference in DIC of more than 10 rules out the model with the higher DIC while with a difference of less than 5 there is no clear winner." (a) shows the distribution of DIC∗ differences between models with nonstationary and stationary ξ over the HRCONUS domain; 99.4% of grid points have values of $|\Delta DIC^*| < 5$, while fewer than 0.03% of grid points have magnitudes that exceed 10. (b) Spatial distribution of posterior probability of an increase in ξ in the nonstationary model; values shown are aggregated 100-km × 100-km grid box means. Statistically significant increases are found at 5.2% of grid points versus decreases at 2.6% of grid points. The mean (median) posterior probability of an increase in ξ is 0.53 (0.52).
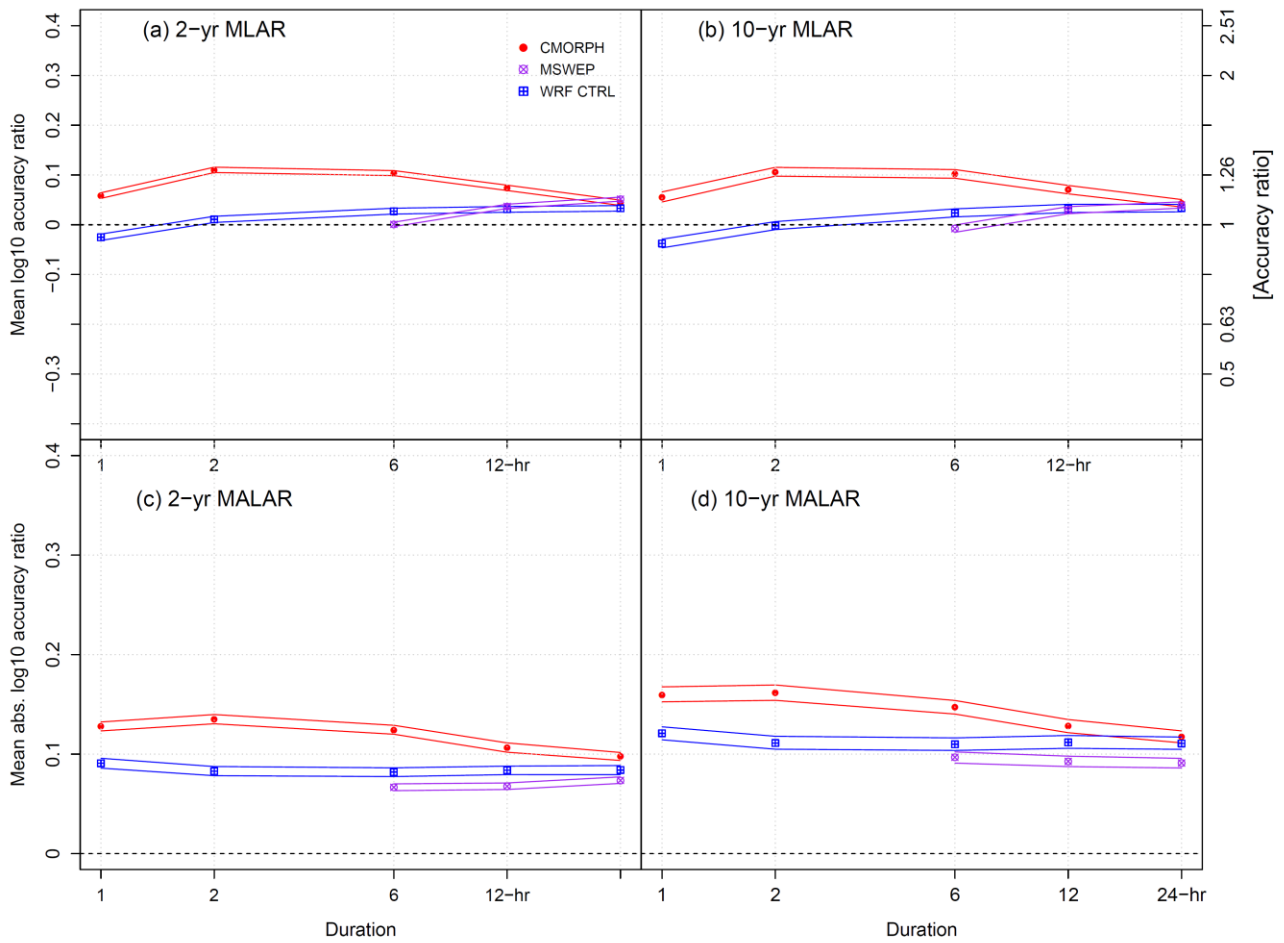
Figure S3: Summaries of MLAR and MALAR for the empirical 50th (2-yr return level) and 90th percentile (10-yr return level) of annual maximum rainfall intensities between each of MSWEP, CMORPH, and WRF CTRL gridded datasets – adjusted to account for area-to-point comparisons using ARFs – and station observations for 1-hr to 24-hr accumulation durations. Solid lines indicate the 95% confidence interval. Perfect performance is indicated by the horizontal dashed lines.
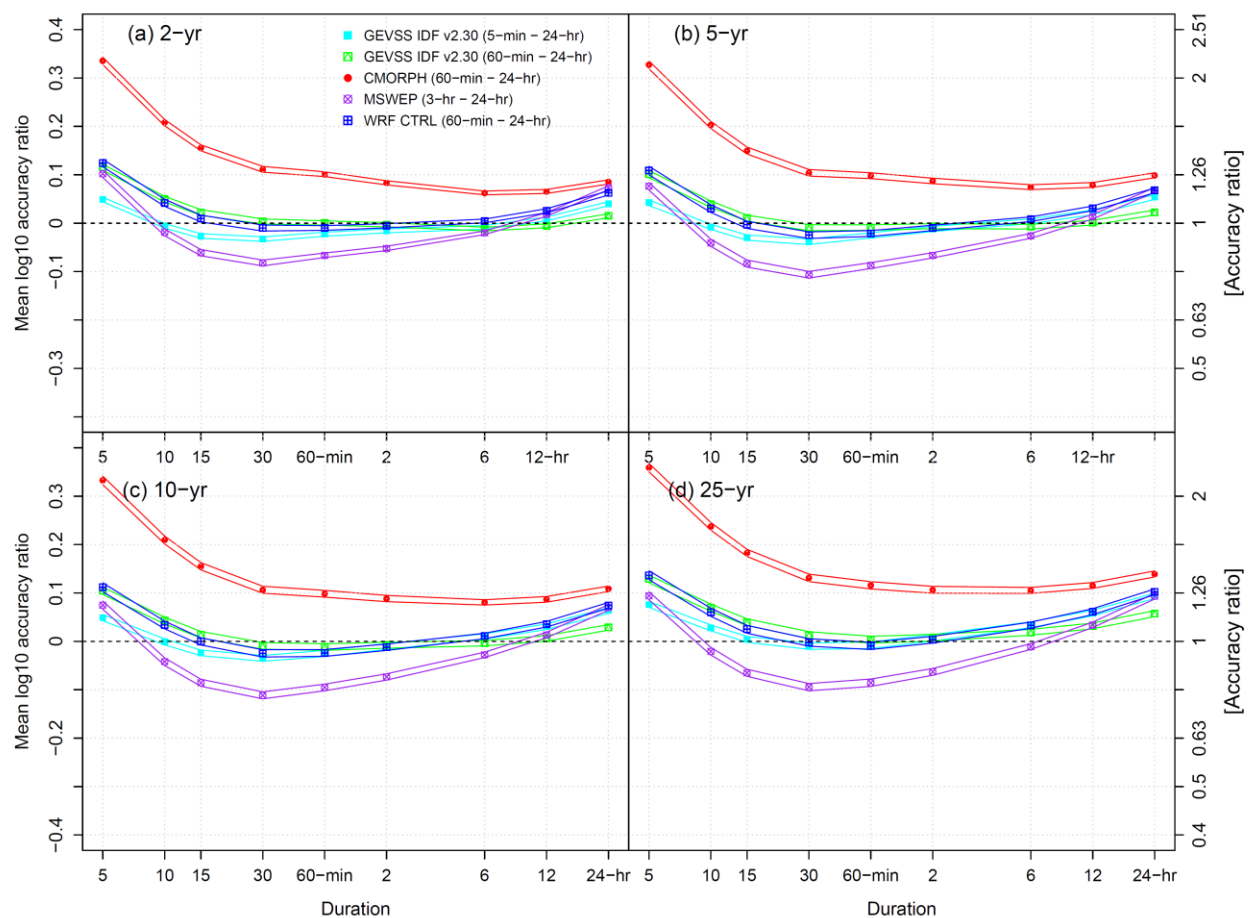
Figure S4: Summaries of MLAR for the GEVSS (a) 50th (2-yr return level), (b) 80th 5-yr return level), (c) 90th (10-yr return level), and 96th (25-yr return level) percentile estimates of annual maximum rainfall intensities for each of MSWEP, CMORPH, and WRF CTRL gridded datasets, all adjusted to account for area-to-point comparisons using ARFs. Solid lines indicate the 95% credible interval. Results are compared with ECCC IDF curves v2.30 estimates for 5-min to 24-hr accumulation durations at 488 TBRG stations. For reference, values are shown for GEVSS IDF curve estimates based on 5-min to 24-hr TBRG data and a restricted set of 60-min to 24-hr durations. Perfect performance is indicated by the horizontal dashed lines.
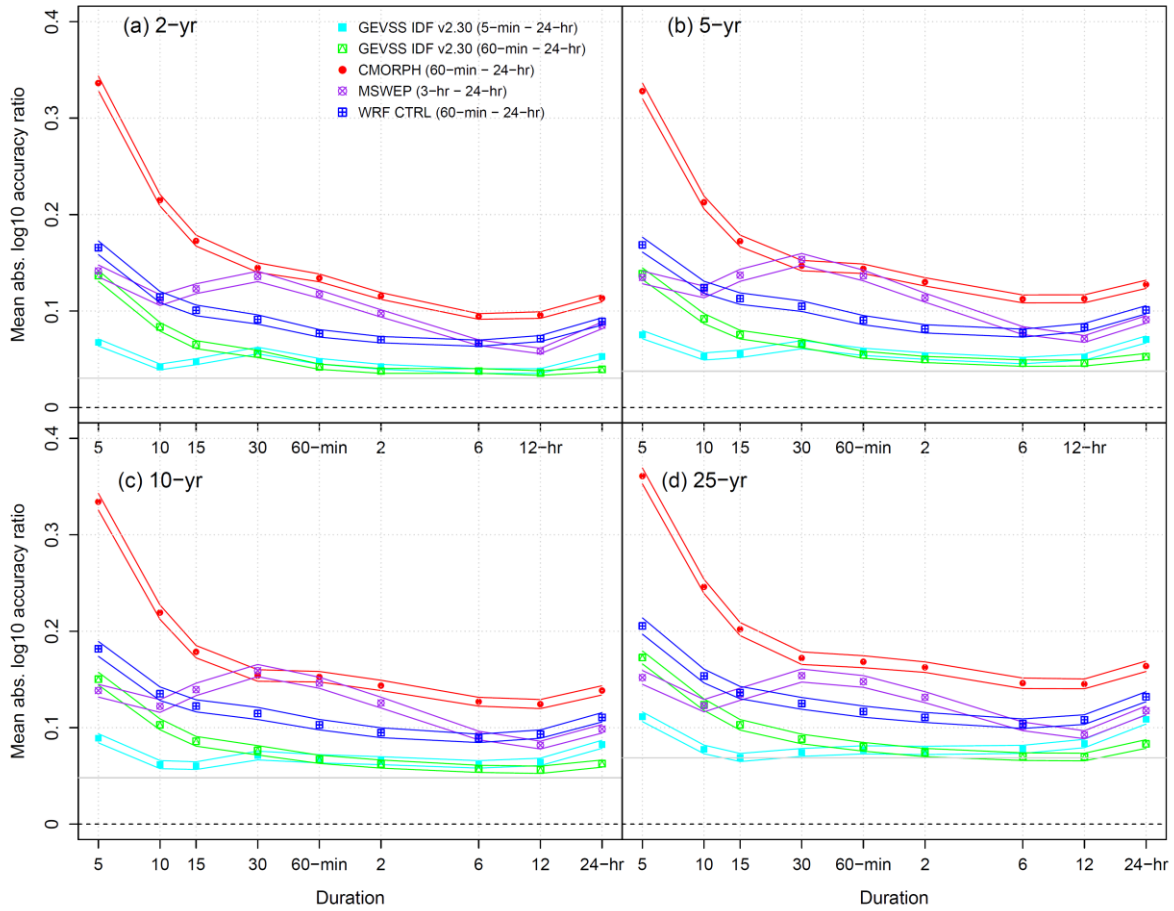
Figure S5: As in Figure S4, but for ARF-adjusted MALAR values. For reference, the horizontal gray line indicates the expected MALAR for empirical quantile estimates, based on 25-yr samples (the median record length of TBRG station observations), from a true $GEV(\mu=1.93, \sigma=0.64$, shape $\xi=0.10)$ distribution; parameters correspond to median estimates at the 488 IDF curve TBRG stations.
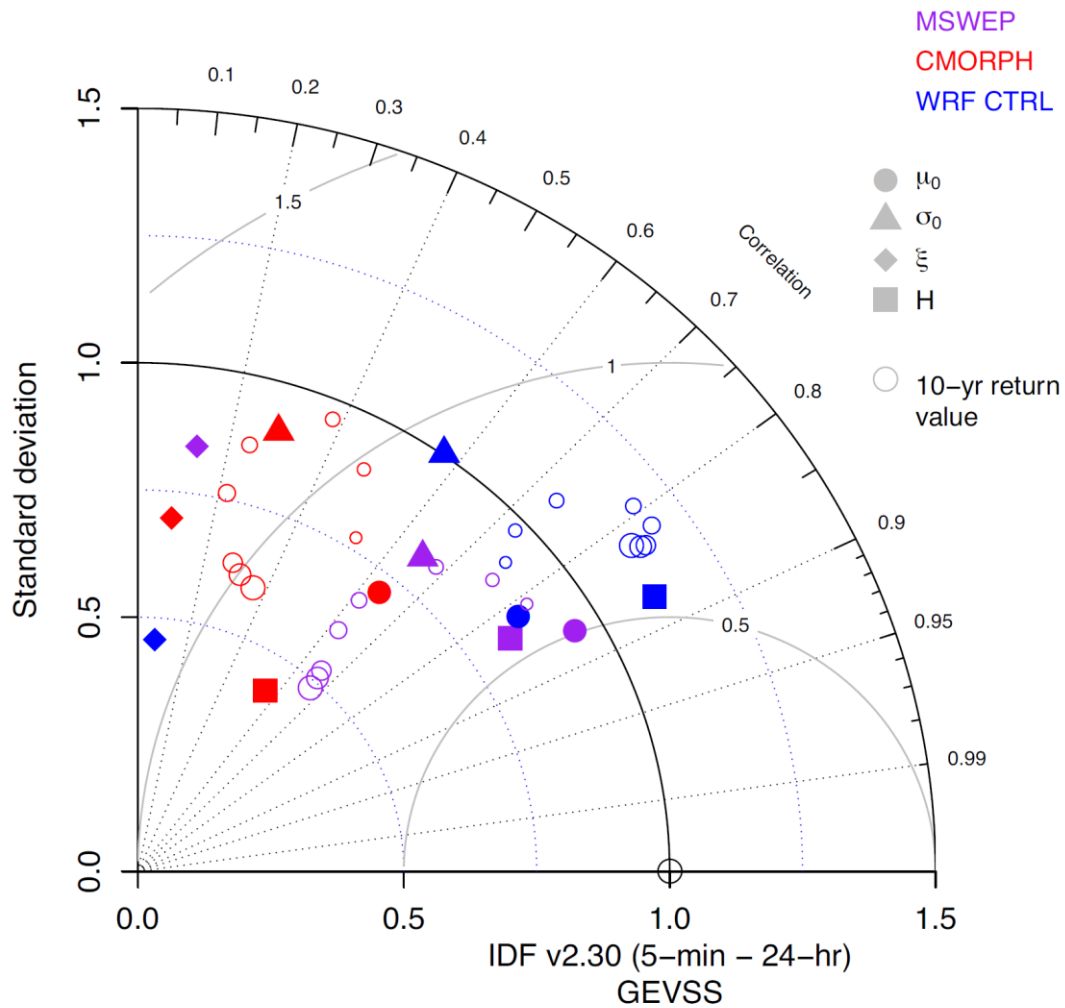
Figure S6: Taylor diagram showing spatial pattern correlations and standard deviations of estimated GEVSS parameters (and 10-yr return levels for different durations – larger open circles indicate shorter durations) for MSWEP, CMORPH, and WRF CTRL at the 488 IDF curve TBRG stations shown in Figure 1. Observational reference values are based on fitting the GEVSS distribution to observed 5-min to 24-hr annual maxima at the TBRG locations. Data are standardized based on the observational reference variability.
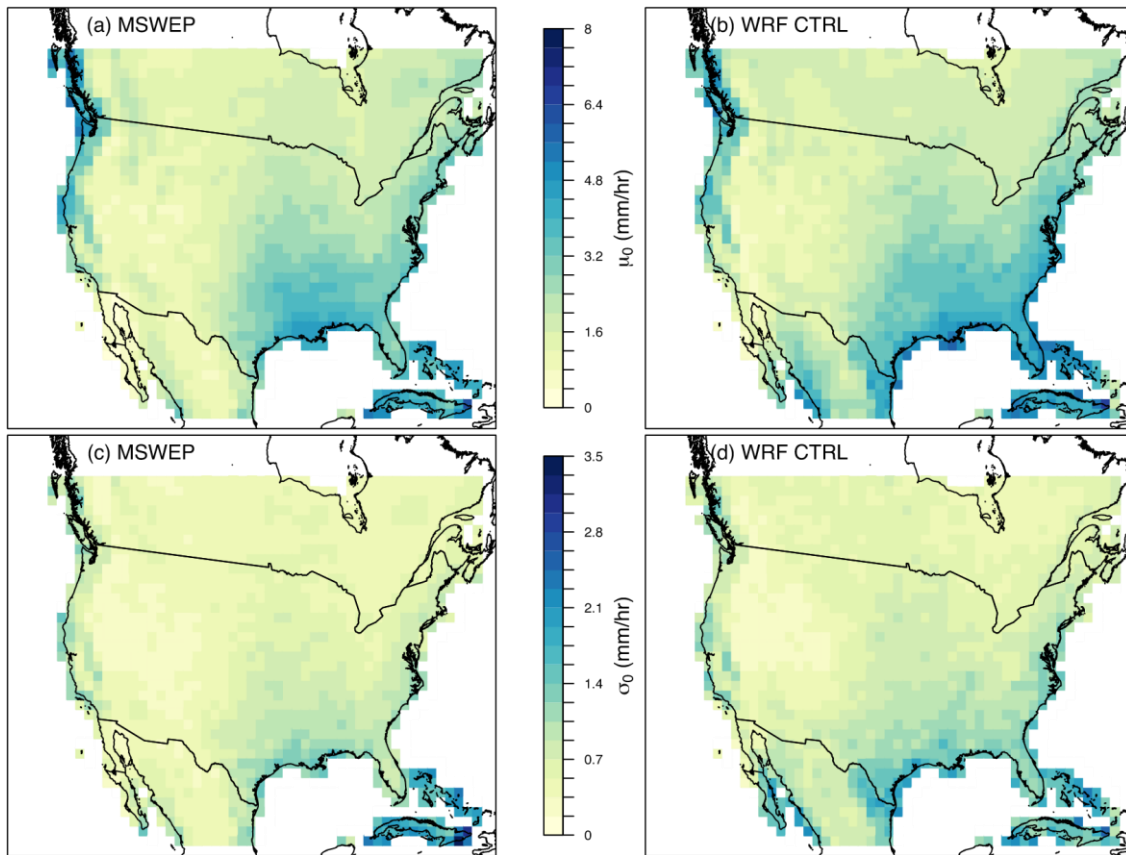
Figure S7: Posterior mean values of the GEVSS location parameter μ_0 for (a) MSWEP and (b) WRF CTRL; and scale parameter σ_0 for (c) MSWEP and (d) WRF CTRL. For ease of visualization, results are aggregated to a 100-km $\times$ 100-km grid. Values shown are aggregated grid box means.
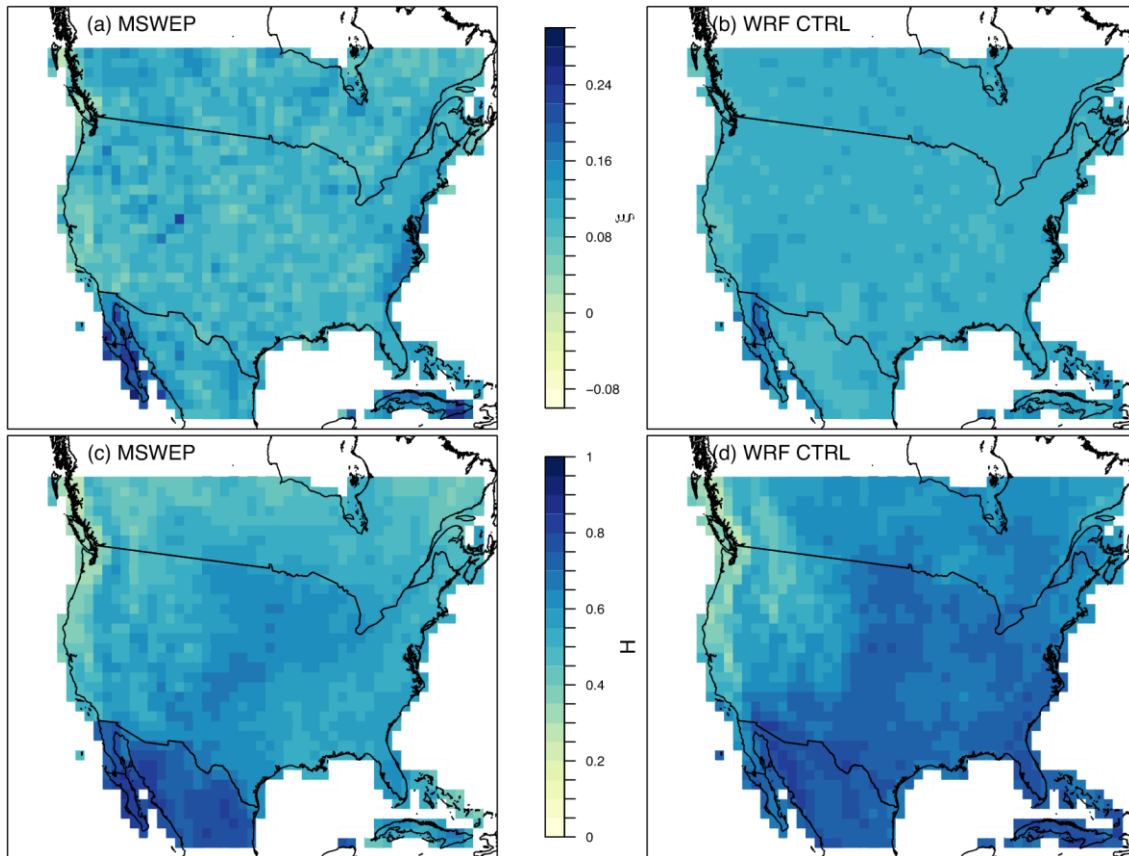
Figure S8: As in Figure S7, but for the GEVSS shape parameter ξ for (a) MSWEP and (b) WRF CTRL, and for the scaling exponent parameter H for (c) MSWEP and (d) WRF CTRL.
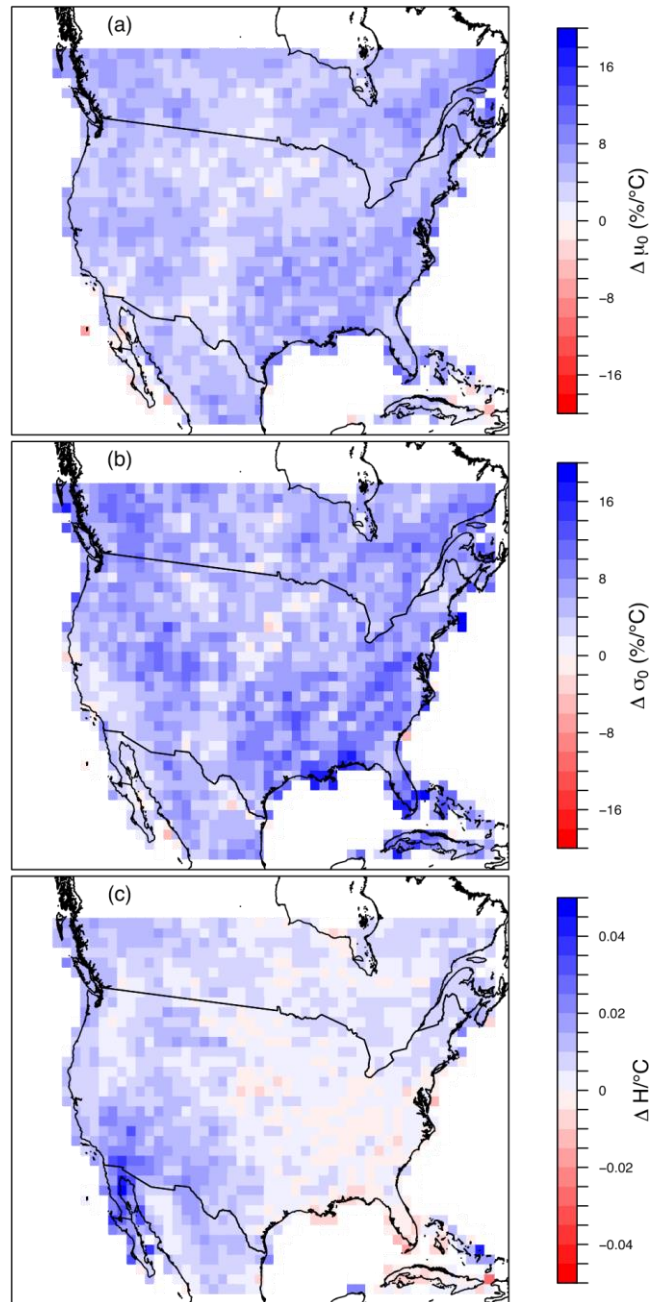
Figure S9: Temperature scaling of GEVSS location μ_0, scale σ_0, shape ξ, and scaling exponent H parameters based on changes between the WRF CTRL and PGW simulations; values shown are aggregated 100-km × 100-km grid box means.